https://doi.org/10.1016/j.cej.2021.130862

In-Situ Observation of the Gas Evolution Process on the Air Electrode of Zn-Air Batteries during Charging

Yi He[a], Wenxu Shang[a], Meng Ni[b,c], Yiyin Huang[d], Hong Zhao[e], Peng Tan[a,*]

a. Department of Thermal Science and Energy Engineering, University of Science and Technology of China, Hefei 230026, Anhui, China.
b. Department of Building and Real Estate, The Hong Kong Polytechnic University, Hung Hom, Kowloon, Hong Kong, China.
c. Environmental Energy Research Group, Research Institute for Sustainable Urban Development (RISUD), The Hong Kong Polytechnic University, Hung Hom, Kowloon, Hong Kong, China.
d. Fujian Provincial Key Laboratory of Quantum Manipulation and New Energy Materials, College of Physics and Energy, Fujian Normal University, Fuzhou 350117, Fujian, China.
e. School of Materials Science and Energy Engineering, Foshan University, Foshan 528011, Guangdong, China.
*Corresponding author: pengtan@ustc.edu.cn (Peng Tan)

Abstract

Although tremendous efforts are made in developing effective bifunctional catalysts of rechargeable Zn-air batteries, the detailed charging process ~~is~~ has been overlooked for a long time. Herein, an insightful investigation of the gas evolution process on the air electrode during charging is performed through in-situ observation, and the effects of different electrode structures and operating conditions are illustrated to optimize the battery performance.

Broader context

Rechargeable Zn–air batteries have attracted worldwide attention, while the development is still in the infant stage. Among various hurdles, the low actual energy density and poor stability are vital to the application. Although tremendous efforts are made in developing stable Zn electrodes and bifunctional catalysts, the processes during the battery operation have been ~~few~~ rarely reported. Herein, an in-depth investigation into the gas evolution on the air electrode is conducted using the in-situ observation technology. It is found that the charging process can be divided into three stages: no obvious bubbles, small bubbles owing to the oxygen evolution, and large bubbles owing to oxygen evolution and gaseous carbon corrosion. When the catalyst loading increases, the bubbles on the surface become smaller and sparser. At low current densities, the air electrode can keep "self-clean" from bubbles, which is the ideal state. Whereas with an increase of the current density, the large bubbles stage is enlarged, and more bubbles are attached to the surface, leading to extra charge impedance. As the discharging depth reduces, the three stages disappear, and only small bubbles can be found on the surface. This work promotes the development of high-performance Zn-air and other metal-air batteries.

Introduction

Rechargeable Zn–air batteries have great advantages in terms of high energy density (1353 Wh

kg^{-1}), low cost (potentially <$10 per kWh), eco-friendliness (free of heavy metal), and excellent safety (aqueous electrolyte, no danger of flammable and explosive), making them as one of the most promising candidates for mobile and portable devices.[1-4] This kind of battery is typically based on an alkaline KOH electrolyte, metallic zinc as the negative electrode, and an air-breathing electrode as the positive electrode.[5] The dissolution and deposition of zinc and the reduction and evolution reactions of oxygen enable the battery to discharge and charge.[6]

However, the practical applications of Zn-air batteries face several issues, such as low actual capacity, poor energy efficiency, and insufficient cycle stability.[7] This is because, on the one hand, the zinc electrode has passivation, dendrites, and hydrogen evolution during the operation, resulting in low zinc utilization and poor cycling stability;[8] on the other hand, the catalyst on the air electrode has insufficient catalytic activity for the electrochemical reactions of oxygen, which directly leads to high overpotential and low energy efficiency.[9] Therefore, a research hotspot in recent years is the design of electrode materials, especially bifunctional catalysts for the oxygen reduction reaction (ORR) and evolution reaction (OER).[10, 11] Among various bifunctional catalysts, carbon materials are usually employed as the support for the dispersion of catalysts and the conductive substrate to boost charge transfer of catalysts.[12, 13] Besides, heteroatom-doped carbon catalysts (e.g., nitrogen-, sulfur-, phosphorus-, or boron-doped carbon) have received great attention as noble-metal-free catalysts.[14, 15]

In rechargeable Zn-air batteries,[16, 17] the charging process includes not only the electrochemical reactions at the interfaces but also bubbles nucleation, growth, desorption, transportation, and other complex processes on the air electrode, which is related to the OER ($OH^- \rightarrow O_2$)[18] and carbon corrosion ($C \rightarrow CO$).[19-21] During the charging processes, a surge in the gaseous oxygen will occur, and over time, the carbon monoxide will also generate and accumulate into bubbles. Once these bubbles cover the surface of the air electrode, it will severely affect the reaction interface and even lead to the failure of the electrode. To this end, timely releasing gaseous oxygen from the air electrode and suppressing carbon corrosion is vital for the stable operation of Zn-air batteries. In this regard, Wang et al.[22, 23] proposed the method of using electromagnetic force to enhance the transport of oxygen bubbles, through which the bubbles could be quickly detached from the electrode surface. Philip et al.[24] found that carbon corrosion could be divided into carbon dissolution and CO evolution, and oxygen evolution and gasification of the carbon to CO would be the dominant processes in carbon black once the charging voltage arrives above the critical value. Although the OER mechanism and process have been investigated in water splitting for a long time,[25-27] the detailed behaviors in rechargeable Zn-air batteries have yet been reported to the best of our knowledge. To push this technology into practical applications, the gas evolution behaviors under different electrode structures and operating conditions should be therefore clarified.

Herein, an in-depth investigation into the gas evolution process on the air electrode during charging was conducted based on benchmark catalysts composed of commercial Pt/C and Ir/C and carbon paper substrate. A home-made Zn-air battery with an optical platform was designed for in-situ observation of the bubble behaviors under different charging currents, catalyst loadings, and discharging depths. This work fills the gap between microscopic catalysts and macroscopic charging behaviors in rechargeable Zn-air batteries and promotes the design of materials and the optimization of operating conditions for metal-air batteries.

The structure of the battery and the in-situ optical platform are illustrated in **Fig. 1a**. The battery contains a zinc plate electrode, an alkaline electrolyte, and an air electrode. The experimental details

(e.g., electrolyte composition, air electrode material, preparation process, optical platform) are presented in **Electronic Supplementary Information (ESI)**. **Fig. S1** presents the discharge and charge polarization curves with different catalyst loadings. With an increase of the loading, the discharging and charging voltages are significantly reduced. **Fig. 1b** displays the voltages curve at 10 mA cm^{-2} for discharging and 70 mA cm^{-2} for charging. An initial discharge process is applied because when the battery is directly charged, due to the low concentration of zinc ions in the electrolyte (0.2 M $Zn(C_2H_5)_2$), water electrolysis will occur instead of the Zn-air battery charging. As shown in **Fig. S2**, the charging voltage curve is completely different from the one shown here. Therefore, only by discharging in advance and then equal-capacity charging can represent the real behaviors in rechargeable Zn-air batteries. The entire charging process on the air electrode is recorded in **Movie S1**, and five photos (Photo 1-5) are presented in the inset of **Fig. 1b** to show different charging stages. In the beginning, the catalyst surface contacts well with the electrolyte (Photo 1). As the charging progresses, oxygen begins to generate based on the OER mechanism:[28]

$$4OH^- \rightarrow O_2 + 4e^- + 2H_2O, E^o = -0.4\ \text{V (vs. SHE)} \quad (1)$$

Because the produced oxygen in this stage is not saturated, it can dissolve into the electrolyte in time[29] or directly escapes into the air through the porous air electrode (**Movie S2** and **Fig. S3**). Thus, no obvious bubbles can be found on the surface (Photo 2). During this stage (Photo 1-2), the two-phase interfaces[30] between the electrolyte and the catalyst has not been stabilized since the charging has just started, and the voltage keeps rising consequently. Then, oxygen continues to accumulate until it reaches saturation and begins to nucleate and appear on the surface of the electrode in the form of small bubbles (Photo 3). Meanwhile, the contact between the two-phase interfaces begins to strengthen, resulting in the slight decrease of the charge voltage (Photo 2-3). After that, the voltage is stabilized while oxygen continues releasing (Photo 3-4). Further, large bubbles begin to generate on the surface with dark brown stripes appear in the electrolyte (Photo 4). This may come from carbon corrosion:[19, 20]

$$C_{(s)} + H_2O \rightarrow CO + 2H^+ + 2e^-, E^o\text{=}0.518\ \text{V (vs. SHE)} \quad (2)$$

and carbon dissolution (organic products appear in the electrolyte). Actually, carbon corrosion has occurred from the beginning of charging. However, due to the catalysis of Ir/C, the carbon corrosion is greatly suppressed by the OER as depicted in **Fig. S4**.[20] As the charging progresses, more and more carbon is corroded. Correspondingly, the electrode surface is partially covered with small O_2 bubbles and large CO bubbles (Photo 4-5). In addition, the organic stripes in the electrolyte become darker and more obvious. With the formation of a large number of bubbles on the porous electrode, the bubble growth forces the electrolyte out of the pores and restricts ionic transport into the interior surface. When the interior surface is isolated from the bulk electrolyte in ions, the reaction interfaces shrink, leading to the rise of the charging voltage. Due to buoyancy, the large bubbles (O_2 and CO bubbles merge into larger bubbles due to surface tension) detach from the electrode surface along the electrolyte injection hole. At this moment, the electrolyte resumes contact with the catalyst, leading to the drop back of the voltage. Meanwhile, the hydrogen evolution on the Zn electrode (**Fig. S5**) also changes its reaction interface, both of which result in the fluctuation of the charging voltage near the end. When the charging is over, the electrode surface is covered by numerous bubbles (Photo 5). **Fig. S6** shows that after charging, plenty of carbon and catalyst particles on the catalyst layer surface fall off, exposing the binder. The catalytic effect is therefore weakened and the carbon corrosion is enhanced, leading to ~~the~~ more violent formation of CO bubbles. According to the above results, the charging process of a Zn-air battery accompanies bubbles generation with three stages:

no obvious bubbles, small bubbles (O_2 bubbles), and large bubbles (O_2 with CO bubbles). In order to avoid the accumulation of bubbles in the battery, we hope that there will be no obvious bubbles during the whole charging process. Thus, the factors related to the gas evolution should be considered carefully, which can be briefly classified into the structure of the air electrode and the operating conditions (i.e., charging current and discharging/charging depth).

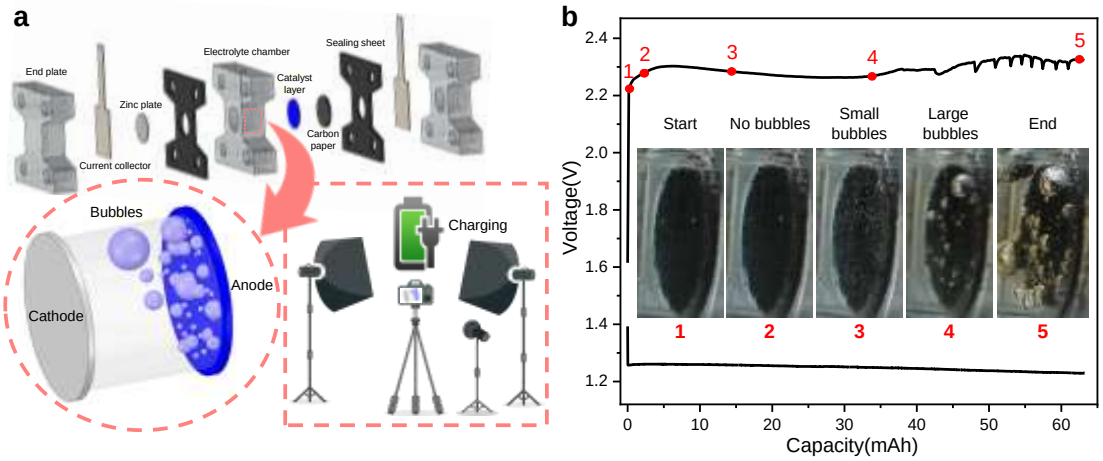

Fig. 1 (a) Schematic illustration of the home-made Zn-air battery and the in-situ optical platform. (b) Galvanostatic discharge at 10 mA cm^{-2} and charge at 70 mA cm^{-2} of the Zn-air battery with the total catalyst loading of 5.35 mg cm^{-2}, and the inset shows the photos of the indicated charging states 1-5.

First, the bubble behaviors under the catalyst loadings of 0.89, 2.29, and 5.35 mg cm^{-2} at the current density of 60 mA cm^{-2} are investigated. The microstructure of the catalyst layers in the air electrode is shown in **Fig. S7**. As the loading increases, the thickness of the catalyst layer also increases from 21.2 to 62.2 and 147.9 μm. On the one hand, the increase in the catalyst loading can effectively increase the reaction area, thereby reducing the overpotential; on the other hand, the thicker catalyst layer will increase the gas transport impedance. As shown in **Fig. 2a**, the charging voltage decreases significantly with the loading increases, indicating that the overpotential increase due to increased gas transport ~~impedance~~ resistance is relatively small compared to the overpotential reduction due to the increase in the reaction area. The entire charging processes are recorded in **Movie S3**, and four corresponding photos at different states of charge (SOC) are presented in **Fig. 2b-d**. As the loading increases, the generation time of large bubbles (i.e., CO bubble nucleation time) on the air electrode delays significantly, as indicated in **Fig. 2a**. The bubble generation also becomes more peaceful, and the bubbles on the electrode become smaller and sparser, which is conducive to reducing the bubble adhesion impedance. Meanwhile, the dark-brown stripes in the electrolyte become more slight. Thus, more OER catalyst is favorable for stable charging, which can not only promote oxygen releasing rather than accumulating on the electrode surface but also suppress carbon corrosion.

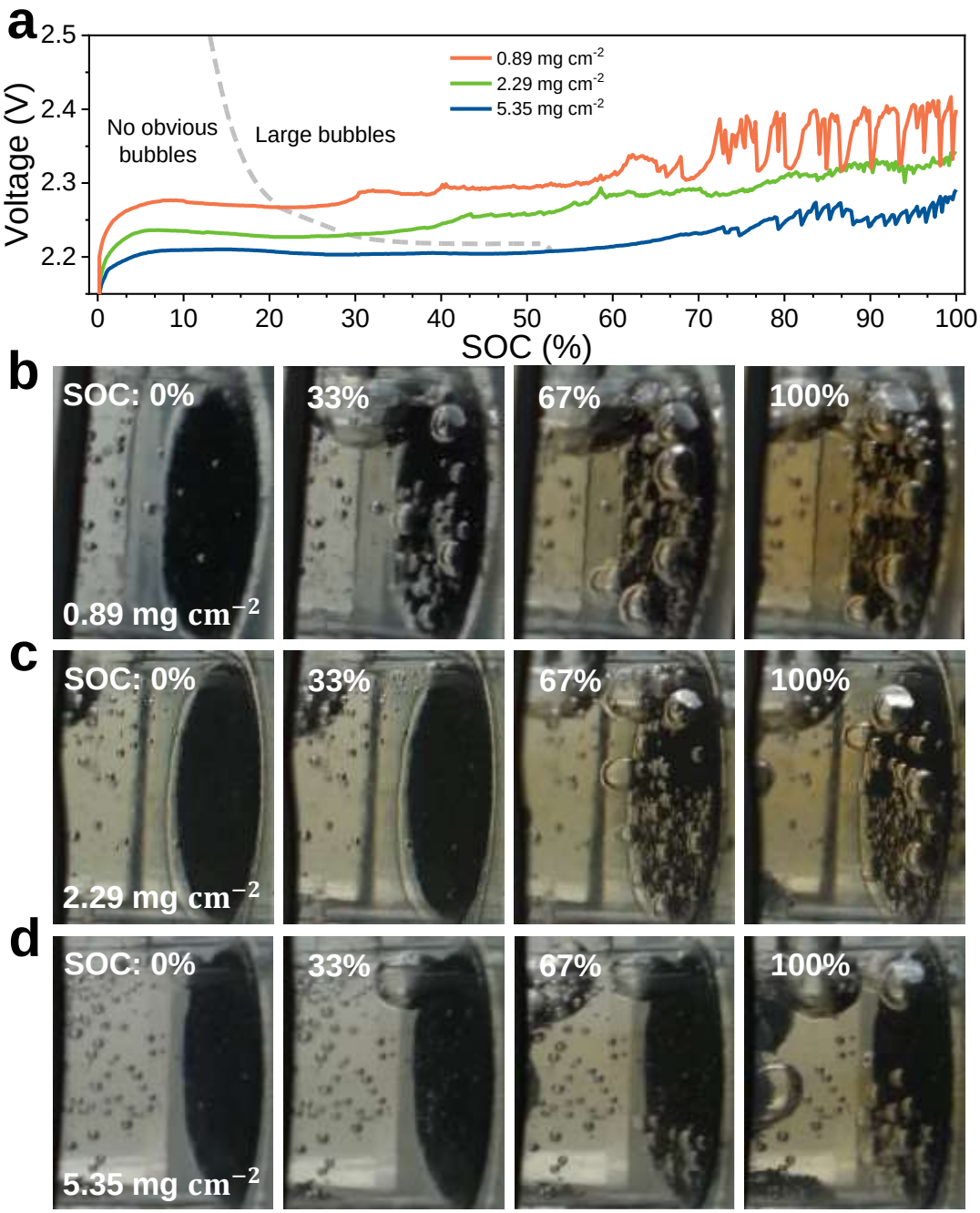

Fig. 2 (a) Galvanostatic voltage curves of the Zn-air battery under different catalyst loadings at the charge current density of 60 mA cm^{-2}. (b-d) Photos of the air electrode with the catalyst loading of (b) 0.89, (c) 2.29, and (d) 5.35 mg cm^{-2} under different SOC.

Based on the catalyst loading of 5.35 mg cm^{-2}, the bubble behaviors at different current densities ranging from 30 to 70 mA cm^{-2} are investigated. **Fig. 3a** shows the charging voltage curves of the batteries after discharging for 8 hours at 10 mA cm^{-2} (100% SOC) in advance. Although the overpotential increases significantly with an increase of the current density, the starting voltage is still ~2.3 V even at the maximum current density of 70 mA cm^{-2}, indicating the remarkable OER activity of Ir/C. The five charging processes under different currents are recorded in **Movie S4**, and four photos corresponding to different states are presented in **Fig. 3b-f**. Interestingly, at the low current densities of 30 and 40 mA cm^{-2}, no obvious bubbles can be observed until the end of charge,

and only dark-brown stripes due to carbon corrosion are found in the electrolyte, indicating that the produced gas (O_2 and CO) is either dissolved in the electrolyte or transported to the outer atmosphere in time (**Fig. 3b** and **3c**). Actually, this current density is much higher than those applied in rechargeable Zn-air batteries,[31-33] which maybe the reason that the gas evolution behaviors have been few focused on in previous research. When the current density further increases, the three stages (i.e., no bubbles, small bubbles, and large bubbles) indicated in **Fig. 1b** begin to appear. The photos in **Fig. 3d, e,** and **f** show the beginning of the charge, the end of the first stage, the end of the second stage, and the end of the entire charging with indicating the corresponding SOC. As the current increases, the SOC of each stage-ending is lower, namely, the nucleation of O_2 and CO bubbles on the air electrode is advanced. Meanwhile, as shown in the last photos and **Movie S4**, the generation of bubbles on the electrode surface also becomes more violent. Further combining with the charging curves (**Fig. 3a**), the voltage gradually increases after the small bubbles stage, which is mainly related to the impedance of bubble adhesion. Based on the above results, the stage accompanying CO bubbles due to carbon corrosion will be enlarged with an increase of the current density. In addition, more bubbles (O_2 and CO) will adhere to the electrode surface, which seriously affects the charging performance of the battery.

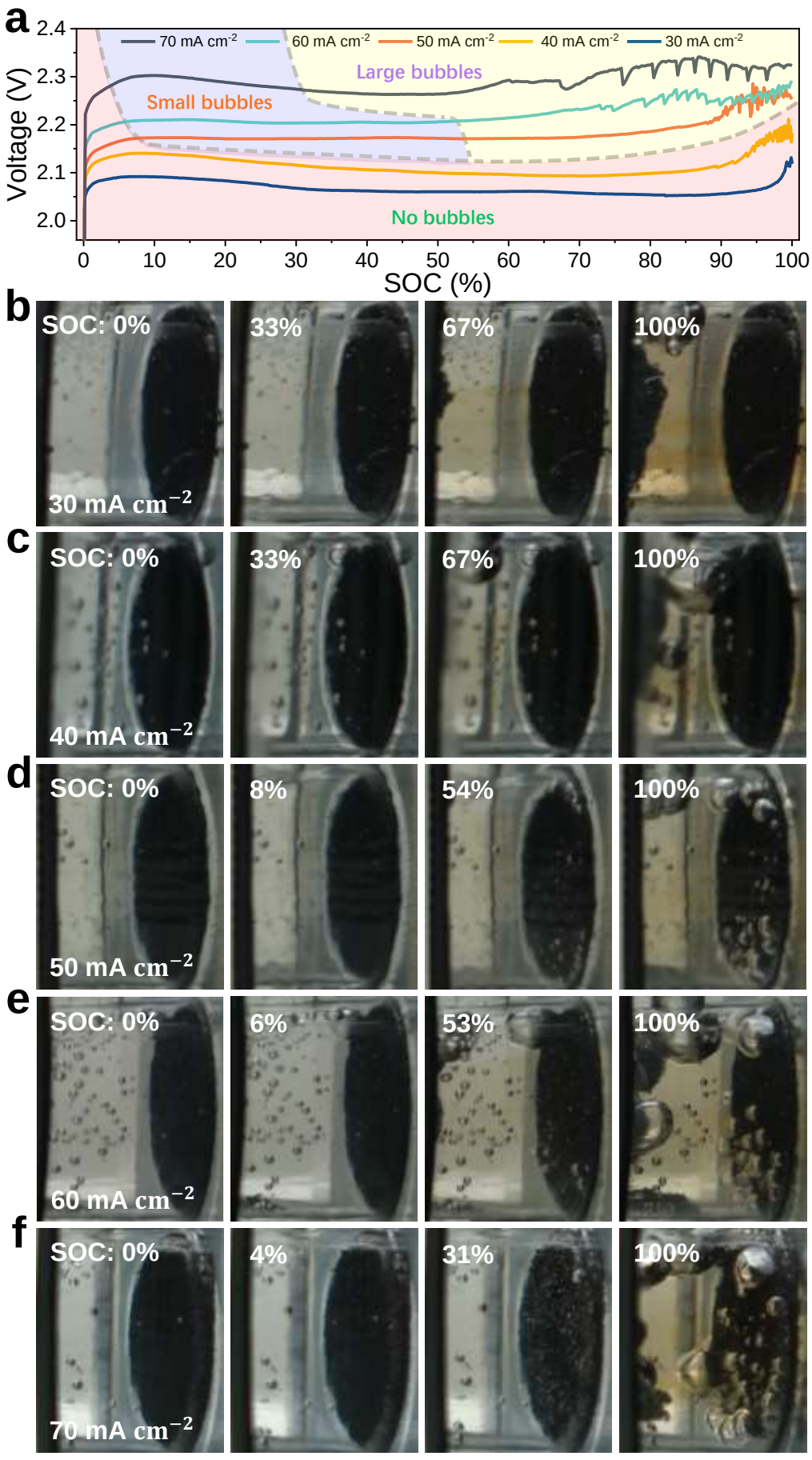
a
Voltage (V)
SOC (%)
70 mA cm-2
60 mA cm-2
50 mA cm-2
40 mA cm-2
30 mA cm-2
Small bubbles
Large bubbles
No bubbles
b
SOC: 0%
33%
67%
100%
30 mA cm−2
c
SOC: 0%
33%
67%
100%
40 mA cm−2
d
SOC: 0%
8%
54%
100%
50 mA cm−2
e
SOC: 0%
6%
53%
100%
60 mA cm−2
f
SOC: 0%
4%
31%
100%
70 mA cm−2

Fig. 3 (a) Galvanostatic charge voltage of the Zn-air battery at different current densities under the catalyst loading of 5.35 mg cm^{-2}. (b-f) Photos of the air electrode during the charging process at the current density of (b) 30, (c) 40, (d) 50, (e) 60, and (f) 70 mA cm^{-2}.

At a given electrode and current density, the discharge/charge depth is usually correlated to the cycling stability.[34, 35] To this end, the bubble behaviors are also expected to be different under different depths. **Fig. 4a** presents the discharge-charge curves of the batteries with the capacities of 31.6, 47.4, and 63.2 mAh. When setting the capacity of 63.2 mAh as 100% depth, the other two are marked as 50% and 75% depth, respectively, as indicated in **Fig. 4a**. As the depth increases, the charging voltage decreases, which is related to the lower concentration polarization due to the increase of the zincate ion concentration in the electrolyte. The entire charging processes are recorded in **Movie S5,** and four photos corresponding to different SOC are presented in **Fig. 4b-d**. Under the 100% discharging depth, the three stages appear on the electrode surface. However, when reducing to 75%, only small bubbles appear on the surface with no nucleation of CO bubbles throughout the charging process. The surface can therefore keep relatively clean. As the depth further decreases to 50%, smaller and sparser bubbles are observed. This may be because at a lower discharging depth, the charging time becomes shorter (due to the same charging current density). In this case, the generated O_2 and CO can be released in time instead of forming bubbles. Thus, the low discharge/charge depth is favorable for the stable operation of rechargeable Zn-air batteries. In most reported Zn-air batteries, the time of one discharge-charge cycling is generally less than 20 min[36-38]. Although the pulse-current method can be applied to demonstrate the catalyst stability, such a short time with the low depth will cause a waste of Zn capacity and is impracticable for applications. Therefore, to achieve a rechargeable Zn-air battery with a high capacity and cycling stability, the air electrode should be well design to suppress carbon corrosion and facilitate oxygen releasing, which will be our next research topic.

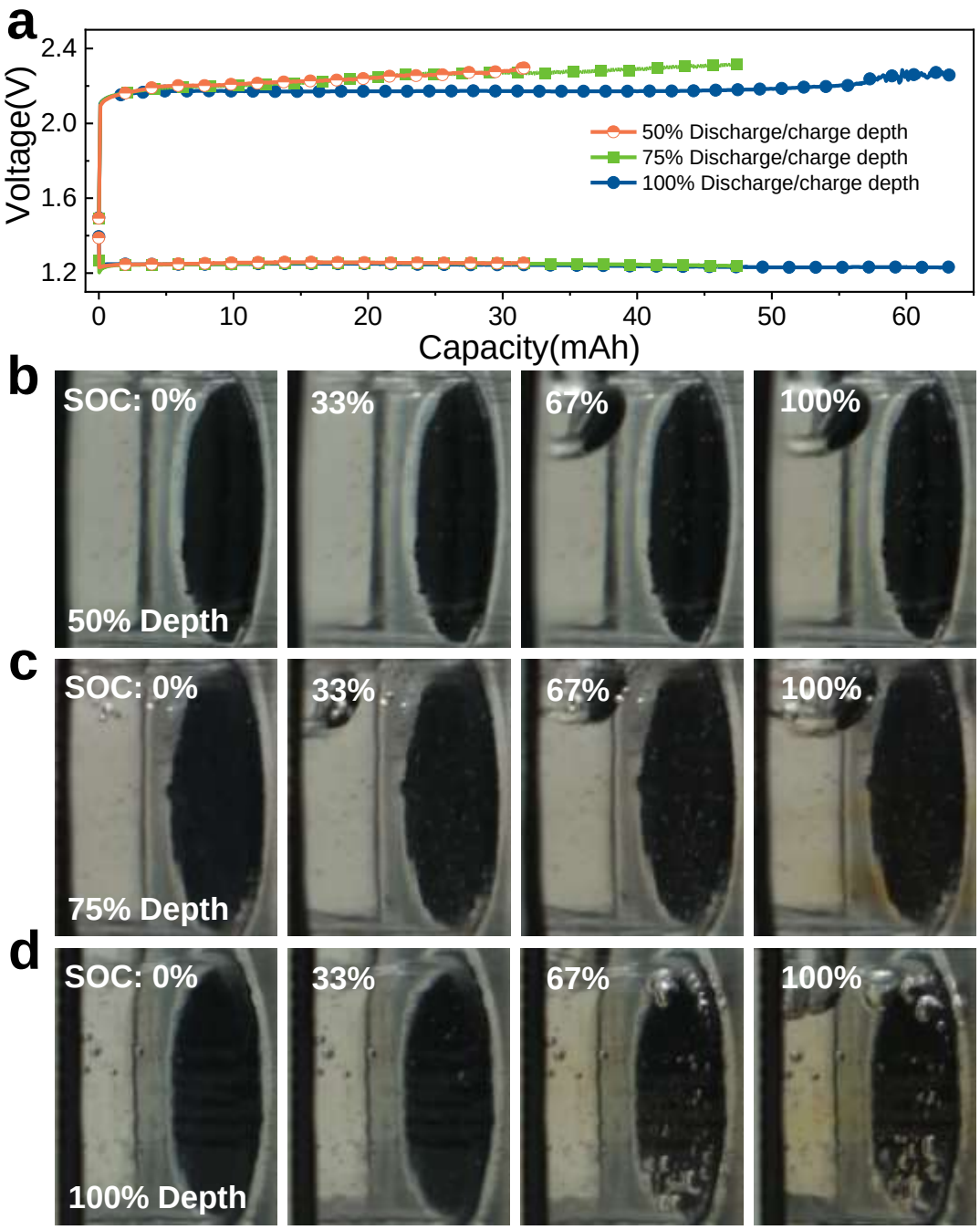

Fig. 4 (a) Galvanostatic voltage curves of the Zn-air battery under different discharge/charge depths with a catalyst loading of 5.35 mg cm^{-2} at 10 mA cm^{-2} for discharging and 50 mA cm^{-2} for charging. (b-d) Photos of the air electrode during the charging process under the discharge/charge depth of (b) 50%, (c) 75%, and (d) 100%.

In summary, an in-depth investigation into the gas evolution process on the air electrode of Zn-air batteries during charging has been carried out. The bubble behaviors under different catalyst loadings, current densities, and discharge/charge depths are in-situ observed, and the results are schemed in **Fig. 5**. The charging process of the Zn-air battery accompanies bubbles generation, and the process can be divided into three stages: no obvious bubbles stage, O_2 bubbles stage (small bubbles, OER), and O_2 and CO bubbles stage (large bubbles, OER with carbon corrosion). As the catalyst layer thickness increases, the nucleation time of large bubbles on the surface extends

significantly. Meanwhile, the bubble generation also becomes more peaceful, and the bubbles become smaller and sparser, which reduces the bubble adhesion impedance. At the low current densities, the air electrode can keep "self-clean" from bubbles, which is the ideal state for the charging process. With an increase of the current density, the large bubbles stage is enlarged with more bubbles attach to the surface, leading to extra charge impedance. When the discharge/charge depth reduces, the three-stage of bubbles disappears, and only small bubbles can be found on the surface instead. Meanwhile, the generated bubbles also become smaller and sparser since the accumulated O_2 and CO (if any) are not enough to nucleate or grow up in such a short time. Therefore, properly increasing the catalyst loading with the reduction of current density and discharge/charge depth may be beneficial to keep the air electrode surface in a satisfactory condition. However, to achieve a high capacity and cycling stability, the air electrode should be well design to suppress carbon corrosion and facilitate oxygen releasing. This work will favor shaping future research toward the development of practical rechargeable Zn–air batteries with superior performance and extended lifetime.

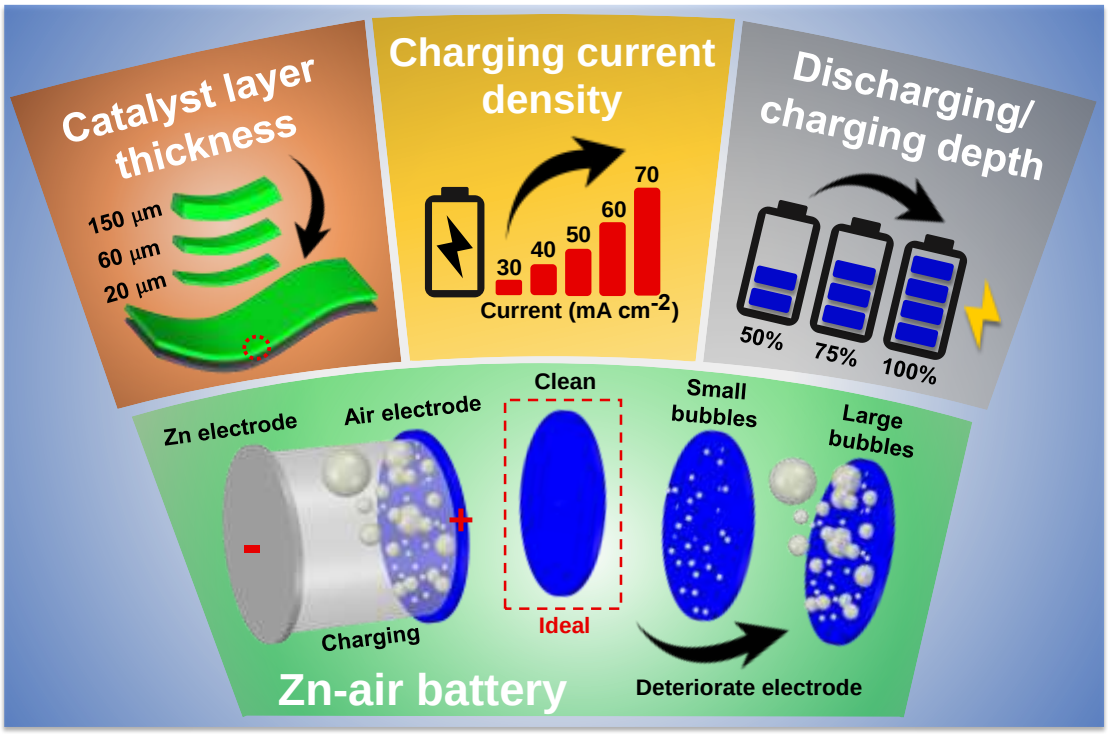

Fig. 5 Scheme of bubble behaviors under different catalyst loadings, charging currents, and discharging depths on the air electrode of Zn-air batteries during charging. The arrow indicates the tendency of the electrode to gradually deteriorate.

Acknowledgments

P. Tan thanks the funding support from Anhui Provincial Natural Science Foundation (2008085ME155), USTC Research Funds of the Double First-Class Initiative (YD2090002006), CAS Pioneer Hundred Talents Program (KJ2090130001), Joint Laboratory for USTC and Yanchang Petroleum (ES2090130110), and USTC Tang Scholar (KY2090000065). M. Ni thanks the funding support (Project Number: PolyU 152214/17E and PolyU 152064/18E) from Research Grant Council, University Grants Committee, Hong Kong SAR. H. Zhao thanks the funding support from The Guangdong Provincial Education Department Special Project of Key Research Areas

(2020ZDZX2066).

References

1. J. Fu, Z. P. Cano, M. G. Park, A. Yu, M. Fowler and Z. Chen, *Adv Mater*, 2017, **29**.
2. J. Yi, P. Liang, X. Liu, K. Wu, Y. Liu, Y. Wang, Y. Xia and J. Zhang, *Energy & Environmental Science*, 2018, **11**, 3075-3095.
3. J. Zhang, Q. X. Zhou, Y. W. Tang, L. Zhang and Y. G. Li, *Chem Sci*, 2019, **10**, 8924-8929.
4. W. Shang, W. Yu, Y. Liu, R. Li, Y. Dai, C. Cheng, P. Tan and M. Ni, *Energy Storage Materials*, 2020, **31**, 44-57.
5. J. W. Zhou, J. L. Cheng, B. Wang, H. S. Peng and J. Lu, *Energ Environ Sci*, 2020, **13**, 1933-1970.
6. T. P. Zhou, N. Zhang, C. Z. Wu and Y. Xie, *Energ Environ Sci*, 2020, **13**, 1132-1153.
7. W. Shang, W. Yu, P. Tan, B. Chen, Z. Wu, H. Xu and M. Ni, *J Mater Chem A*, 2019, **7**, 15564-15574.
8. L. Zhang and Y. Hou, *Adv Energy Mater*, 2021, DOI: 10.1002/aenm.202003823.
9. J. Yan, Y. Wang, Y. Zhang, S. Xia, J. Yu and B. Ding, *Adv Mater*, 2021, **33**, e2007525.
10. F. Pan, Z. Li, Z. Yang, Q. Ma, M. Wang, H. Wang, M. Olszta, G. Wang, Z. Feng, Y. Du and Y. Yang, *Adv Energy Mater*, 2020, **11**.
11. E. Davari and D. G. Ivey, *Sustainable Energy & Fuels*, 2018, **2**, 39-67.
12. W. Wu, Y. Liu, D. Liu, W. Chen, Z. Song, X. Wang, Y. Zheng, N. Lu, C. Wang, J. Mao and Y. Li, *Nano Research*, 2020, **14**, 998-1003.
13. L. Zou, C. C. Hou, Q. Wang, Y. S. Wei, Z. Liu, J. S. Qin, H. Pang and Q. Xu, *Angew Chem Int Ed Engl*, 2020, **59**, 19627-19632.
14. K. Zeng, X. Zheng, C. Li, J. Yan, J.-H. Tian, C. Jin, P. Strasser and R. Yang, *Adv Funct Mater*, 2020, **30**.
15. S. S. Ren, X. D. Duan, S. Liang, M. D. Zhang and H. G. Zheng, *J Mater Chem A*, 2020, **8**, 6144-6182.
16. H. Tabassum, A. Mahmood, B. J. Zhu, Z. B. Liang, R. Q. Zhong, S. J. Guo and R. Q. Zou, *Energ Environ Sci*, 2019, **12**, 2924-2956.
17. X. C. Chen, Z. Zhou, H. E. Karahan, Q. Shao, L. Wei and Y. Chen, *Small*, 2018, **14**.
18. P. Tan, B. Chen, H. Xu, H. Zhang, W. Cai, M. Ni, M. Liu and Z. Shao, *Energy and Environmental Science*, 2017, **10**, 2056-2080.
19. S. Möller, S. Barwe, S. Dieckhöfer, J. Masa, C. Andronescu and W. Schuhmann, *ChemElectroChem*, 2020, **7**, 2680-2686.
20. S. Moller, S. Barwe, J. Masa, D. Wintrich, S. Seisel, H. Baltruschat and W. Schuhmann, *Angew Chem Int Ed Engl*, 2020, **59**, 1585-1589.
21. H. Ohkuma, I. Uechi, M. Matsui, Y. Takeda, O. Yamamoto and N. Imanishi, *J Power Sources*, 2014, **245**, 947-952.
22. K. Wang, X. Liu, P. Pei, Y. Xiao and Y. Wang, *Chem Eng J*, 2018, **352**, 182-187.
23. K. Wang, P. Pei, Y. Pei, Z. Ma, H. Xu and D. Chen, *Sci Rep-Uk*, 2016, **6**.
24. P. N. Ross and H. Sokol, *J Electrochem Soc*, 1984, **131**, 1742-1750.
25. J. S. Kim, B. Kim, H. Kim and K. Kang, *Adv Energy Mater*, 2018, **8**, 26.
26. J. Du, F. Li and L. Sun, *Chem Soc Rev*, 2021, DOI: 10.1039/d0cs01191f.
27. T. X. Nguyen, Y. H. Su, C. C. Lin, J. Ruan and J. M. Ting, *Advanced Science*, 2021, DOI:

10.1002/advs.202002446.
28. Y. P. Deng, R. L. Liang, G. P. Jiang, Y. Jiang, A. P. Yu and Z. W. Chen, *Acs Energy Lett*, 2020, **5**, 1665-1675.
29. N. Staud and P. N. Ross, *J Electrochem Soc*, 1986, **133**, 1079-1084.
30. F. X. Wang, X. W. Wu, C. Y. Li, Y. S. Zhu, L. J. Fu, Y. P. Wu and X. Liu, *Energ Environ Sci*, 2016, **9**, 3570-3611.
31. P. Du, K. Hu, J. Lyu, H. Li, X. Lin, G. Xie, X. Liu, Y. Ito and H.-J. Qiu, *Applied Catalysis B: Environmental*, 2020, **276**.
32. H. Ge, G. Li, J. Shen, W. Ma, X. Meng and L. Xu, *Applied Catalysis B: Environmental*, 2020, **275**.
33. Z. Song, J. Ding, B. Liu, X. Liu, X. Han, Y. Deng, W. Hu and C. Zhong, *Adv Mater*, 2020, **32**, e1908127.
34. M. J. Trahan, S. Mukerjee, E. J. Plichta, M. A. Hendrickson and K. M. Abraham, *J Electrochem Soc*, 2012, **160**, A259-A267.
35. G. CiricMarjanovic and S. Mentus, *J Appl Electrochem*, 1998, **28**, 103-106.
36. A. Sumboja, M. Lubke, Y. Wang, T. An, Y. Zong and Z. L. Liu, *Adv Energy Mater*, 2017, **7**.
37. S. J. Peng, X. P. Han, L. L. Li, S. L. Chou, D. X. Ji, H. J. Huang, Y. H. Du, J. Liu and S. Ramakrishna, *Adv Energy Mater*, 2018, **8**.
38. F. L. Meng, H. X. Zhong, D. Bao, J. M. Yan and X. B. Zhang, *J Am Chem Soc*, 2016, **138**, 10226-10231.